Arabian Journal of Chemistry (2022) **15**, 104084

King Saud University

Arabian Journal of Chemistry

www.ksu.edu.sa
www.sciencedirect.com

ORIGINAL ARTICLE

Carbon-dot confined in graphene-analogous boron nitride for enhanced oxidative desulfurization

Toktam Pedram-rad [a], Zarrin Es'haghi [a,*], Ali Ahmadpour [b], Malihe Samadi Kazemi [d], Ali Akbar Mohammadi [c]

[a] *Department of Chemistry, Payame Noor University (PNU), 19395-4697, Iran*
[b] *Department of Chemical Engineering, Faculty of Engineering, Ferdowsi University of Mashhad, Iran*
[c] *Department of Environmental Health Engineering, Neyshabur University of Medical Sciences, Neyshabur, Iran*
[d] *Department of Chemistry, Faculty of Sciences, Bojnourd Branch, Islamic Azad University, Bojnourd, Iran*

Received 16 April 2022; accepted 26 June 2022
Available online 3 July 2022

KEYWORDS

Graphene-like boron nitride;
C-nanodot;
Dibenzothiophene;
Fuel oil

Abstract As of late, graphene-like boron nitride (g-BN), has been created another schedule as aerobic catalysis, and have a profound effect on the key performance of the catalyst. In this paper, C-nanodots with low resistivity, were bounded through g-BN (C-dots/g-BN) to help electron versatility by a straight forward one-pot pathway. C-dots were bounded in graphene-analogous boron nitride (g-BN) via a one-step, in situ process at increased temperature, which could upgrade the interactions of C-dots and control the dimensions of C-dots in the scope of nearly 4–5 nm. The results demonstrated that C-dots/g-BN has a superior execution in high-impact oxidation of dibenzothiophene (DBT) in fuel oil with a reactant movement of 93.5%. Estimation showed that hydroxyl radicals produced from H2O2 as a result of the interaction with C-dots ended up a proficient catalyst in the framework. The C-dots had a synergetic impact to enhance the proficiency of H2O2 in the catalyst. The portrayal results showed that piece of the DBT was oxidized to its comparing sulfoxide which requires less oxidant than sulfone. Both of the oxidation items could be extracted in the oil phase on the catalyst.

1. Introduction

Other strategies are essential to reach the concentration of sulfur in fuel with a safe content, e.g. lower than 10 ppm (Rappas, 2002). Oxidative desulfurization (ODS) is viewed as a hopeful and novel technique for very profound desulfurization of fuel. Contrasted and ordinary reactant hydrodesulfurization (HDS), ODS can be completed under extremely gentle situations: at room temperature and under climatic weight. Amid oxidative desulfurization as well as sulfuric natural mixtures can be oxidized by the electrophilic increase of oxygen particles with the sulfur iotas to shape sulfoxides and sulfones. The concoction

* Corresponding authors.
E-mail addresses: zeshaghi@pnu.ac.ir (Z. Es'haghi), mohammadi.eng73@gmail.com (A.A. Mohammadi).
Peer review under responsibility of King Saud University.

Production and hosting by Elsevier

https://doi.org/10.1016/j.arabjc.2022.104084
1878-5352

and physical things of sulfoxides and sulfones are essentially not the same as those of hydrocarbons in fuel oil, and thusly they can be expelled by refining, dissolvable extraction subsequent dissolvable extraction utilizing water-dissolvable polar solvents, for example, NMP, DMF, DMSO, etc. (Rappas, 2002), or adsorption. Scheme 1 demonstrates the oxidation of natural sulfur mixes. By blend of the procedures, the sulfur-containing substances of the diesel might be decreased to 50 ppm (Sampanthar et al., 2004).

Aerobic catalysis, a cost-effective and high-dynamic strategy, has for quite some time been exceedingly looked for after by researchers (Miyamura et al., 2015; Xu et al., 2015; Yu and Cohen, 2015; Huang et al., 2014; Zhong et al., 2015; Liu et al., 2016). In the previous a couple of years, honorable metals, (for example, Au (Yu and Cohen, 2015; Huang et al., 2014; Zhong et al., 2015; Liu et al., 2016; Zhang et al., 2015; Hinde et al., 2015; Zhu et al., 2013), Pt (Tu and Chin, 2015; Yang et al., 2013) and Pd (Yang et al., 2013; Huang et al., 2013) and so on.) have been viewed as compelling channels to this objective, however constrained by their staggering expenses. Moreover, carbon-based impetuses (counting carbon nanotubes, graphene, and so on.) additionally have been intended for high-impact catalysis, and amazing exhibitions have paid back (Huang et al., 2013; Jawale et al., 2015; Wen et al., 2015). All the more as of late, as a similarity to graphene (Pakdel et al., 2014; Liu et al., 2015; Weng et al., 2014; Xiong et al., 2015), we understand other 2D substances, graphene-like boron nitride (g-BN), can likewise work as an ease and great-effective impetus for catalysis (Wu et al., 2016) Like graphene, g-BN shows great mechanical quality and thermal conductivity (Corso et al., 2004) yet higher compound steadiness. Graphene-analogue boron nitride (g-BN) nano sheets have attracted greatly consideration because of their momentous things (Zhi et al., 2013; Dean et al., 2010), for example, an extensive energy band gap (Nag, 2010), top thermal conductivity (Zhi et al., 2009), significant chemical endurance (Xiao et al., 2016), elevated surface area (Weng et al., 2013; Liu et al., 2015) and remarkable adsorption performance (Lei et al., 2015; Xiong et al., 2015; Huang et al., 2018), and extraordinary interlayer structure. Besides that, nitride nanosheets could enhance thermal and mechanical features of adsorbent.

Carbon-based materials have been used as catalysts in several processes because they have appropriate properties such as mechanical and thermal stability, adaptable surface area, and porosity (Meng et al., 2022; Chen et al., 2021; Liu et al., 2015).

Carbon dot is one of the carbon-based nanoparticles with a size of < 10 nm, have become gradually popular in the last years due to its exclusive electrical and optical and properties.Carbon dots can lift photograph actuated electron exchange after mixing with g-BN. Likewise, C-dots bring about special up change features, which implies changing over at least two low-vitality siphon photographs to a higher-vitality yield photo. Furthermore, the stacking of C-dots could advance the mix of oxygen and the animated electron, along these lines enhance the photocatalytic hydrogen generation effectiveness (Tian et al., 2009).

C-dots could be applied as a way for the vehicle of charge transporters, to mix with oxygen. In addition, C-dots have likewise been utilized as a fantastic help for nucleation and development of the perfect nanocrystals because of the oxygen-containing utilitarian gatherings at first glance (Kannan et al., 2015). In C-dots there are carboxylic and hydroxyl bonds through which superb water solvency and additionally biocompatibility are provided. Also, the bands participate in catalyst stability. Considering previous studies on catalyst projects, the application of C-dots as strong supports for the catalysis framework has been less considered (Xu et al., 2004). Strong connections among supports and C-dots could make appropriate characteristics for the catalytic activity and dependability in a chemical reaction. Thus, the coordinate addition of C-dots via g-BN to acquire g-BN-kept (C-dots/g-BN) was carried out by a basic technique. As of late, C-dots are defined as another form of carbon structure with intriguing effects that were first achieved in the cleansing of single-wall carbon nanotubes (Nag et al., 2010).

The control of C-dots by g-BN could lead to better scattering and strength of C-dots. Contrasted and g-BN. The upgraded catalytic reactant action is observed to be established in the enhanced electron mobility by presenting C-dots. Here, C-dot was used as a catalytic developer in the synthesized impetus to enhance the usage proficiency of H2O2 by providing one extra course for improving the effective application. Hence, we coated the C-dots on expelled sulfur compounds. When C-dots are limited in the g-BN structure, the electron movement is obviously improved. The g-BN surface area activated by a catalyst does not decrease because of the ultra-minor size of C-dots, and consequently, the performance of the catalytic can be improved. The system is apprehended by utilizing C-dots accompanied by nano-sizes in the structure of g-BN (C-dots/g-BN). In comparison to g-BN, the C-dots/g-BN displays an advanced operation for oxidizing aromatic sulfur compounds with H2O2. The catalytic action is proven to be origins in the enhanced mobility of electrons by raising C-dots. The C-dots/g-BN showed a high level of activity to remove aromatic sulfur from fuels.

In the present study, the targets of this examination were performed to indicate the role of C-dots on the surface area of g-BN for the adsorption of DBT and also to examine the impact of C-dots loading on the aperture of the g-BN for the first time.

Carbon dots have a number of superior properties such as excellent photostability, biocompatibility, small size, good water solubility in order to use in bio-applications, easily functionalize with modifiers. A novel graphene-like BN modified with C-dots was prepared for the first time via a simple process in this research with the assistance of urea. It was found that the mechanical stability of BN is quite different from that of C-dots/g-BN. BN-carbon dots, as the new BN nanomaterials, with extremely high surface/volume ratios. They have shown very valuable catalytic effects in desulfurization in this research. Many valuable properties of this material are yet to be clarified and therefore are expected to stimulate a lot more theoretical and experimental study.

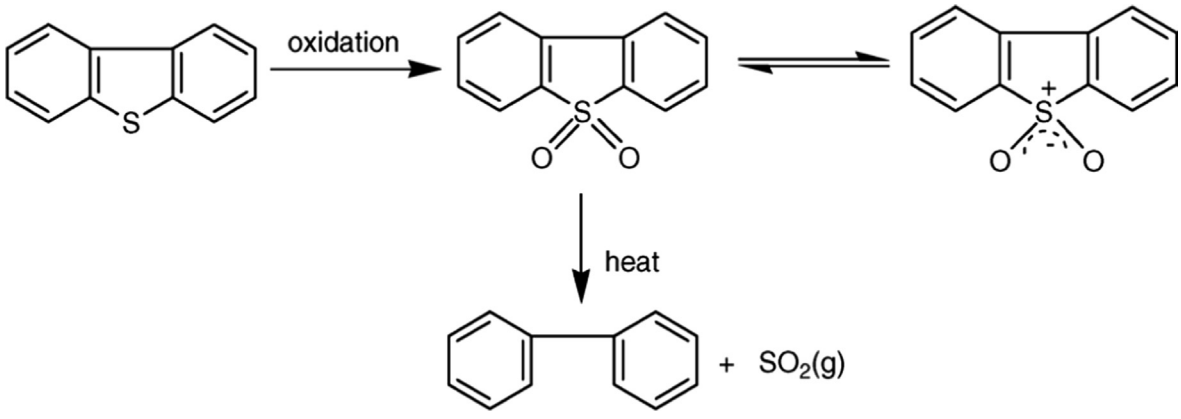

Scheme 1 Oxidation process of natural sulfur.

2. Experimental section

2.1. Material

Boric acid (H_3BO_3), urea (CO $(NH_2)_2$, citric acid, hydrogen peroxide (H_2O_2, 30 wt%), n-heptane, Dibenzothiophene (DBT, 98%), and methanol all were bought from the company of Sigma-Aldrich (USA) without more purifying.

2.2. Report of characterization

A UV-2450 UV/Vis spectrophotometer (Shimadzu, Japan) was used to measure diffuse reflectance UV–Vis (DR-UV–Vis) in the spectrum of 200–800 nm. Also, the photoluminescence emission spectrum was obtained from a fluorescence spectrophotometer (SHIMADZU RF5301-PC).

A Fourier transform infrared (FTIR) spectroscopy modeled Nicolet 560 operated in a transmission state, was employed to define the surface properties of magnetic nanoparticles. FTIR spectra were collected in transmission mode using the KBr pellets in the frequency range of 4000–500 cm^{-1}. The morphologic properties of the nanocomposites applied in this study were examined by field emission-scanning electron microscope (FE-SEM). Also, the characteristics of adsorbents including surface area, pore diameter, and pore volume, as well as the nature of the adsorbents were tested by SEM. Transmission electron microscopy (TEM) images were reached out by a JEOL JEM-2100 TEM at an accelerating voltage of 200 kV. Raman spectra were obtained using a Jobin-Yvon Labram spectrometer.

The structure of the crystalline adsorbents was verified by powder X-ray diffraction installed in a Siemens D–500 X-ray diffractometer fitted with Ni–filtrated CuKα radiation (40 kV tube voltage, 100 mA tube current, and $\lambda = 0.154$ nm, Shimadzu, Japan). The analyses were carried out by Statistical Software (Minitab version 16, Minitab Inc.).

2.3. Preparation of samples

2.3.1. Synthesis of g-BN

Urea and boric acid with a molar ratio of 0.1: 2.4 were dissolved in 40 mL of ultra-pure water. The solution was heated in a water bath to 45 °C until a green–blue solid formed and then collected. The residue was then transferred to a furnace and heated to 900 °C at an inclination rate of 5 °C per minute. This step was performed under N_2 atmosphere (Gholinejad et al., 2016). Urea did not show any structural change up to 100 °C. When the temperature rose to 200 °C, the urea turned into a polymer. (C3H3N3O3, JCPDS Card No. From 23 to 1637). Once the response temperature was increased to 300 °C, the boron nitride was formed.

2.3.2. Synthesis of C-dots

The mixture of Citric acid and urea (1 and 0.5 g, respectively) were dissolved in ultra-purified water (25 mL), and the mixture was heated at 160 °C for 6 h in a Teflon autoclave. At that point, the temperature of the reactor was cooled to RT, and the obtained mixture was centrifuged at 10000 rpm for 10 min to remove solids (Wang et al., 2011).

2.3.3. Synthesis of C-dots/g-BN

Arrangement of C-dots/g-BN is followed by adding C-dots solution with a molar ratio of 0.1: 2.4: 0.000123 in execution time synthesis g-BN (Wang et al., 2011).

2.4. Oxidation of aromatic sulfur compound average sulfur oxidation process

The oil samples utilized for analyses were set up by dissolving DBT in n-heptane and reaching out a 100-ppm sulfur solution. In run-of-the-mill desulfurization oxidation, 0.01 g of catalyst was added to 20 mL modeled oil in a 50 mL flask, and 0.1 mL 30 wt% H2O2. Then the solution was agitated in a thermostatic oil bath of 120 °C to remain unsettled for 180 min.

Models from the upper liquid phase of the reaction were occasionally pulled back and centrifugation separated in advance to measure sulfur content. The concentration of DBT in modeled oil was tested in an UV–Visible spectrophotometer (At a wavelength of 325 nm).

g-BN displays a relation with low activity of catalytic which provides approximately 60% of sulfur reduction under the reaction circumstances and reaction factors. C-dots/g-BN could raise the activity in the catalytic to >98%. It is representative of the introduction of C-dots enhancing electron movement efficiency and increasing the catalytic activity of C-dots/g-BN. Desulfurization ratio was calculated by the following equations:

$$\text{Desulfurization ratio } (\%) = [(C_0 - C)/C_0] \times 100$$

where C_0 is the initial molar concentration of sulfur (mol/L), and C is that of sulfur at the end of the reaction (mol/L). When the reaction is completed, all DBT has been reduced from the oil phase and only the catalyst phase oxidation product will remain. It is demonstrating that all DBT was oxidized to DBTO2.

3. Results and discussion

3.1. Characterization of adsorbent

FT-IR spectra of C-dots/g-BN were conducted to analyze the native forms (Fig. 1). In FT-IR spectra, both examples show properties peaks of about 804 cm^{-1}, resulting in transverse optional B—N in-plane methods and N—B vibration extending modes respectively (Peak et al., 2003) and could provide one active IR peak (1500–1300 cm^{-1}) for unequal B—O and asymmetric B—O stretching bands (1100–950 cm^{-1}) for inactive or weak IR active (related to molecular misshaping) presented by scanning electron microscopic observation (Wang et al., 2015). Bands at 3200–3600 cm^{-1}, are determined as the stretching pulses of hydroxyl groups. It is presented that carboxylate with negative electricity and hydroxyl groups place mostly on the surface area of C-dots (Calvaruso et al., 2001). A number of wide peaks have been detected in the region between 3000 and 3500 cm^{-1}, O—H and N—H frequencies that stretch vibrations, respectively. The NH2 monomeric urea stretching band is characterized by two strong and sharp components, 3440 and 3548 cm^{-1}. The CH stretching band is in the region between (2860, 2960 cm^{-1}) (Gaddam et al., 2014). In the spectrum FTIR (Fig. 1) the C—O stretching frequency is also present at 1124 cm^{-1}. The detection of a peak at 1630 cm^{-1} can be

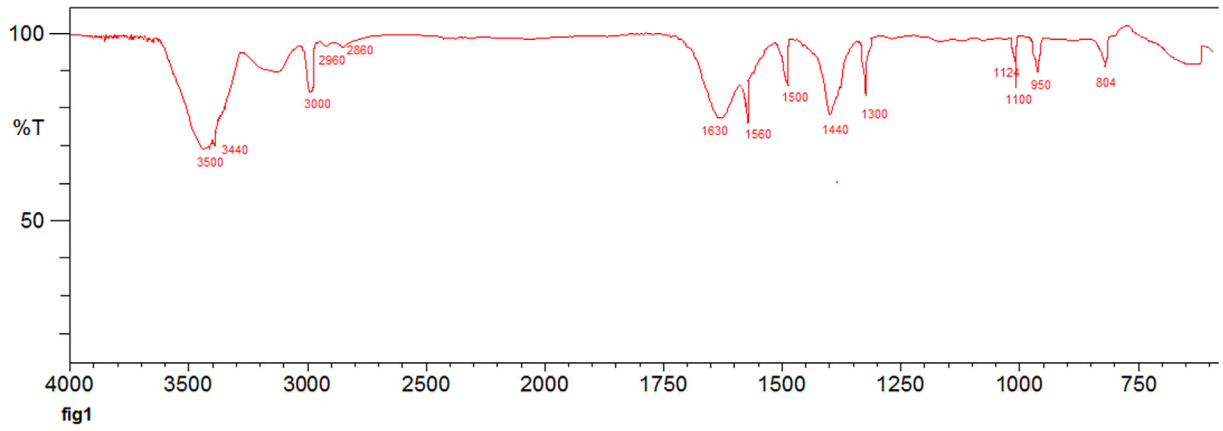

Fig. 1 FT-IR spectra of C-dots/g-BN.

associated with the frequency of C═O aromatic carbonyl stretching; also two peaks were observed at 1440 and 1560 cm^{-1}, which might be derived from the existence of aromatic C═C (Lian et al., 2012).

Fig. 2 displays the crystallographic construction of the organized models in the 2θ range of 10°–80°. The XRD analyzes are used for the analysis of the structure (crystal alignment, phase analysis, grain dimensions, and steady grid factors by precision of ±0.01 μA) of the doped pristine, and metallic carbonates g-BN consequences recorded are completely contrasted to the initial XRD patterns of the standard peaks of hBN (ICDD card no: 34-421) in (Fig. 2a) where g-BN phase attribute peaks are labeled as the Miller Indices (*hkl*). Two wide peaks made at 2θ = 25.68 and 2θ = 42.48 were related to the (002) and (100) crystal planes of BN (JCPDS card No. 34-0421). The (002) peak was apparent as the interplanar wide range of aromatic components and the (100) peak was attributed to the structural pressing theme in the plane, which reflected the successful synthesis of g-BN (Chen et al., 2004). The expulsion of cross-section nitrogen could prompt a more extensive appropriation scope of the separations between strands. Thus, the demand for the strands was remarkably declined, which leads the low intensity of the peaks. After loading the C-dots, the potency of both diffraction peaks declined (Fig. 2b). The presence of C-dots may disturb the polycondensation of urea and the stacking of g-BN sheets. Illustrating a few-layer graphene structure. XRD graph of C-dots indicating the presence of an intensified peak at 2θ = 24.7° and a frail peak at 2θ = 43.3° that are linked to (002) and (100) diffraction models of graphitic carbon individually. This distortion of the crystal lattice can also cause deformities in C-dots.

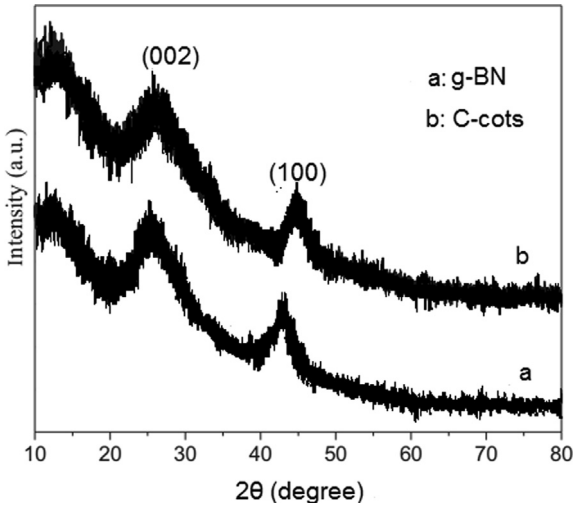

Fig. 2 2a. XRD spectra of g-BN, 2b. XRD spectra of C-dots.

SEM and TEM graphs of the catalysts were revealed in Fig. 3. From the acquired SEM of g-BN, (Fig. 3a) we discovered that the arranged g-BN display a typical layer form of graphene-analogous material. The permeable structure of the carbon nitride could be watched. In (Fig. 3b, 3c) morphologies of all C-dots/g-BN are similar to g-BN. The sizes of C-dots particles were unpredictably placed on the exterior of g-BN, also the previous investigations demonstrated that various nanoparticles can be discovered in C-dots/g-BN. Ultrafine nanoparticles can be discovered by diameters less than 20 nm.

The morphology of the C-dots is explored by TEM. Observation of C-dot particles with unpredicted sizes and shapes in the C-dots solution, proposing the effective union of C-dots. From (Fig. 4a), it tends to be observed that the as-blended C-dots are uniform in size and have an about round shape and it is characteristic of their undefined nature and with widths inside 5 nm. In (Fig. 4b) C-dots are obviously limited through g-BN, prompting high level of security and having a layer structure.

The characteristic peak of Raman spectra at 1376 cm^{-1} is related to the B—N vibration mode (E2g) in g-BN (Gholinejad et al., 2016). While C-dots present the D-band about 1314.63 cm^{-1} and G-band at 1586.27 cm^{-1}. The intensity ratio of the D and G bands (ID/IG) could be explained by the extent of disorder and the ratio of carbon atoms calculated as sp3/sp2 (Weng et al., 2014). C-dots/g-BN, both the characteristic c-dot and g-BN peaks can be discovered. The results of over two spectroscopies show that C-dots are distributed on the exterior layer of g-BN and their structures are maintained from another aspect in the synthesis process. To confirm whether the presentation of layer (Sainsbury et al., 2012). From the information obtained using Raman spectra(Fig. 5), a comparative end to that dependent on the XRD examples could be explained that C-dots are very scattered in g-BN (Baker and Baker, 2010).

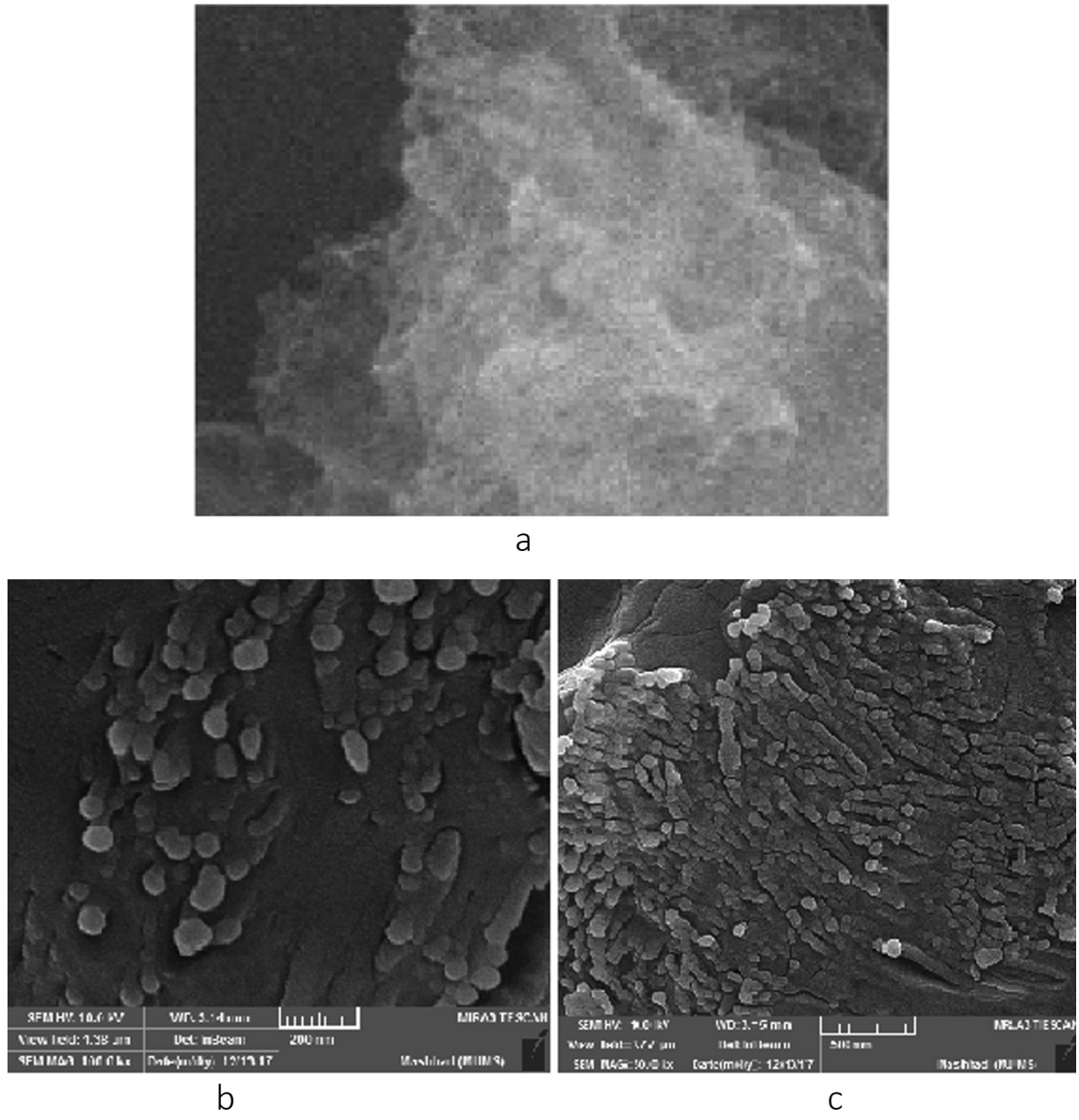

Fig. 3 3a. SEM of g-BN, 3b, 3c. SEM of C-dots/g-BN.

3.2. Fluorescence spectroscopy

The C-dots solution displays strong splendid blue luminescence under simulation of 365 nm, which might be viably observed with a propelled camera. The peaks of C-dots could be identified at different wavelengths from 300 to 440 nm. Fluorescence property is a vital parameter for C-dots which is basic toward the further application (Fig. 6) demonstrates the fluorescence wavelength spectra of the C-dots, C-dots have a strong blue photoluminescence of 450 nm with a full width of up to half (FWHM) as low as 60 nm. It is possible that by expanding of excitation wavelength, the power of luminescence increase to the greatest excitation (340 nm). The utmost thickness at half-maximum is around 68 nm. The peaks can not to change, demonstrating that the luminescence birthplace of C-dots may be not quite the same as most different C-dots that demonstrate the wavelength subordinate fluorescence. The highest wavelength at various excitation conditions stays at 448 nm. In this way, 340 nm is chosen as the wavelength for the going with experimentations (Pan et al., 2010). From the FTIR examination unmistakably the C -dots are ended with a carboxyl gathering at first glance. As a result, the fluorescence characteristics normally alter when they react with metal particles.

3.3. UV–Vis spectroscopy analysis

Furthermore, UV–Vis ranges were likewise utilized for the portrayal of g-BN and C-dots/g-BN (Fig. 7). Intense tops at 240 nm were observed in both the g-BN and C-dots/g-BN spectra, which further indicate that g-BN forms were not pulverized (curve1). The C-dots arrangement holds a maximum absorption at 340 nm and an element at 235 nm in the UV–Vis absorption range of C-dots (curve2), which could be

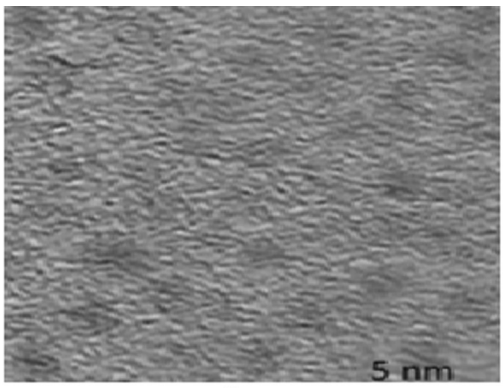

Fig. 4 4a. TEM of C-dots, 4b. TEM of C-dots/g-BN.

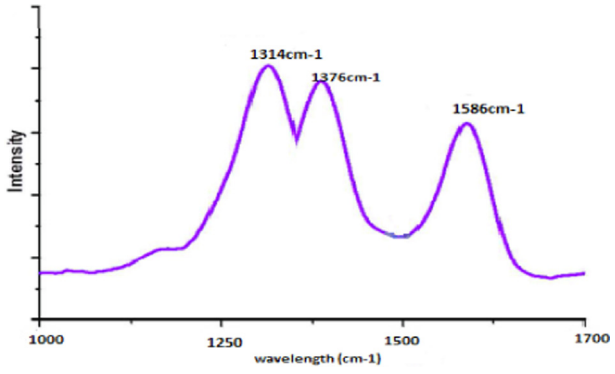

Fig. 5 Raman spectra of C-dots/g-BN.

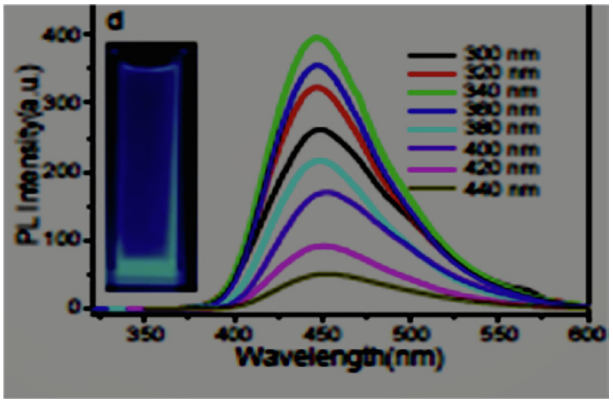

Fig. 6 Fluorescence emission spectra of C-dots.

related to the π-π* change of nanocarbon (Zhang and Wang, 2018).

3.4. Proposed reaction mechanism

Concerning the mechanism of the reaction, UV–Vis spectra were performed. Firstly DBT can be homogenized in the oil phase, while DBT and DBTO2 tend to be in the catalyst phase. Using C-dots, electron mobility could be advanced in relation to reaction rate.

C-dots might catalyze the oxidation of DBT with H2O2. That could be credited to the ·OH species produced from the interaction between C-dots and H2O2 (Kennedy and Krouse, 1999).

Based on the above-mentioned analysis, the reaction steps are proposed as follows: First, adsorption of DBT and O2 (H2O2) onto the surface of C-dots/g-BN; Extension of the bond length of O-O, then, O2 is adsorbed onto g-BN. Therewith, the sole pair electrons on S made in DBT (or 4,6-DMDBT) transfer to adsorbed-O2 via C-dots. The activated C-dots connect to the S atom to formulate sulfoxide. Next, another oxygen atom also connects to an S atom similarly. Then the aromatic sulfur mixtures could be oxidized to corresponding sulfones. It is valuable seeing that C-dots/g-BN dis-

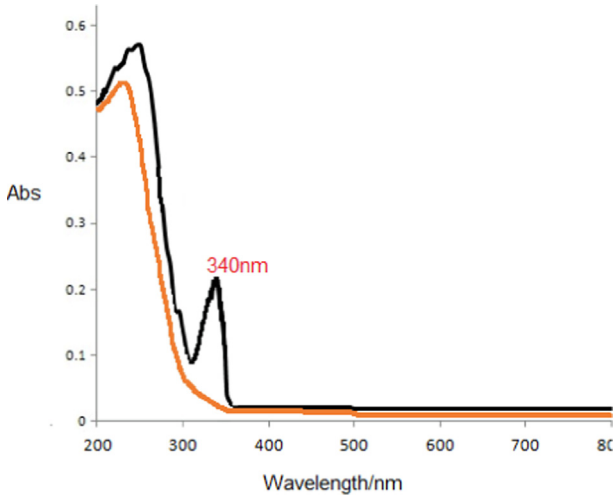

Fig. 7 UV–Vis spectra of C-dots/g-BN.

play a prompter reaction for the reduction of 4,6-DMDBT. It is mainly due to the dissimilarity in electron density of DBT and 4,6-DMDBT (Plackett and Burman, 1946). More densified electrons can carry more lone pair electrons via C-dots and supply more concentration of O2, leading to higher activity (see Scheme 2).

3.5. Experimental design

3.5.1. Screening of significant factors using Plackett-Burman experimental design (PBD)

In this paper, C-dots/g-BN were used and evaluated by experimental design. Although many factors have an impact on this process, some of them have no noteworthy impact on it. Screening plans are utilized to recognize the primary elements and their communications with every single imaginable factor (Sharif et al., 2014). PBD is a beneficial functional design to find important process variables in an experiment (Zolgharnein et al., 2013). So, the screening design was applied mostly. The important factors in the evaluation model can be determined by analyzing the variance (ANOVA) (Tarley et al., 2009). The Placket–Burman (PB) factorial structure can recognize the central point influencing the DBT adsorption and extraction by a generally few examinations. Table 1 demonstrates the test format of the 12-run PBD with reaction esteems (as current pinnacle statures) in two degrees of variables. Following the primer experimentations, the concentration of catalyst, solution volume, temperature, mixing rate, exposure time, n (H2O2)/n (DBT), and amount of C-dots loading with two levels were the considered variables for modified bentonite. The Pareto standardized plots illustrate major PBD effects. The plot of Pareto shows the effects catalyst amount, solution volume, n (H2O2)/n (DBT) and amount loading of C-dots are most imperative to the procedure, these factors should therefore be studied in more noteworthy profundity. Differences in the measured parameters may influence the analytical signal based on the preliminary experiments. The use of central composite design (CCD) was also studied.

3.5.2. Optimization using CCD

The technique used for optimizing the experiment initiated with a screening approach to choose the key parameters and continued with an enhancement structure, for example, the Taguchi plan, CCD, Doehlert grid (DM), or Box-Behnken structure (BBD) (Tarley et al., 2009). In comparison with other methods such as BBD and DM, CCD was shown to be very effective. A CCD consolidates a two-step complete or fragmentary factorial structure with extra focuses (star focuses) and in any event, one point in the focal point of the trial area is chosen to accomplish different properties, e.g. reliability or orthogonal properties. Table 2 displays CCD and current peaks for C-dots/g-BN. The objective of this examination is to augment these assessed reactions to the mean estimation of four signals under the equivalent trial conditions. The reason for this examination is to expand these assessed reactions by applying relapse investigation on test information to the normal estimation of four signals under the equivalent test cir-

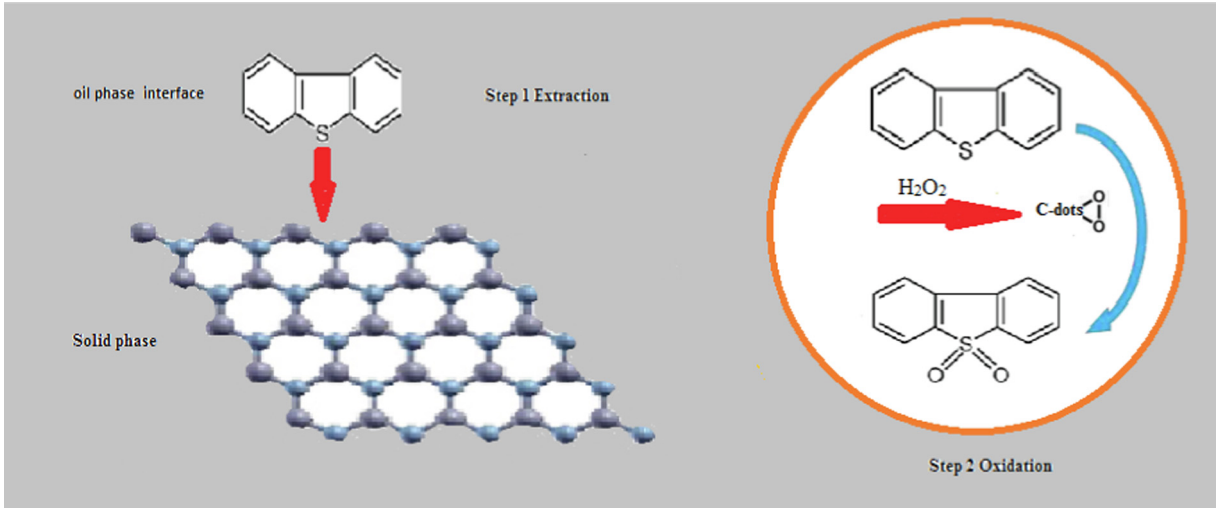

Scheme 2 Proposed mechanism of the oxidative desulfurization of oil mixture by C-dots/g-BN.

Table 1 The results of PB experimental design matrix.

Standard order	Run order	Blocks	Sorbent (g)	volume(ml)	T(°C)	rate(rpm)	time (min)	% amount loading of C-dots	$n(H_2O_2)$/ n(DBT)	A
1	1	1	0.008	5	60	3000	20	0.8	2	0.451
2	2	1	0.008	10	25	5000	20	0.4	2	0.702
3	3	1	0.004	10	60	3000	40	0.4	1	0.454
4	4	1	0.008	5	60	5000	20	0.4	1	0.441
5	5	1	0.008	10	25	5000	40	0.8	1	0.441
6	6	1	0.008	10	60	3000	40	0.4	2	0.591
7	7	1	0.004	10	60	5000	20	0.8	1	0.221
8	8	1	0.004	5	60	5000	40	0.8	2	0.171
9	9	1	0.004	5	25	5000	40	0.4	2	0.211
10	10	1	0.008	5	25	3000	40	0.8	1	0.331
11	11	1	0.004	10	25	3000	20	0.8	2	0.219
12	12	1	0.004	5	25	3000	20	0.4	1	0.291

Table 2 The results of CCD experimental design matrix.

Standard order	Run order	PtType	Blocks	Sorbent amount(g)	solution volume	% amount loading of C-dots	$n(H_2O_2)$/ n(DBT)	A
1	1	1	1	0.006	7	0.6	0.5	1.360
2	2	1	1	0.01	7	0.6	0.5	1.540
3	3	1	1	0.006	7	0.6	1.5	0.961
4	4	1	1	0.01	7	0.6	1.5	1.054
5	5	1	1	0.006	12	0.6	0.5	1.460
6	6	1	1	0.01	12	0.6	0.5	1.640
7	7	1	1	0.006	12	0.6	1.5	0.970
8	8	1	1	0.01	12	0.6	1.5	1.138
9	9	1	1	0.006	7	1	0.5	1.410
10	10	1	1	0.01	7	1	0.5	1.600
11	11	1	1	0.006	7	1	1.5	0.964
12	12	1	1	0.010	7	1	1.5	1.115
13	13	1	1	0.006	12	1	0.5	1.465
14	14	1	1	0.010	12	1	0.5	1.690
15	15	1	1	0.006	12	1	1.5	0.990
16	16	1	1	0.010	12	1	1.5	1.142
17	17	−1	1	0.006	9.5	0.75	1	1.120
18	18	−1	1	0.010	9.5	0.75	1	1.330
19	19	−1	1	0.009	9.5	0.75	0.5	1.490
20	20	−1	1	0.009	9.5	0. 75	1.5	1.011
21	21	−1	1	0.009	7	0.75	1	1.146
22	22	−1	1	0.009	12	0. 75	1	1.261
23	23	−1	1	0.009	9.5	0.6	1	1.201
24	24	−1	1	0.009	9.5	1	1	1.211
25	25	0	1	0.009	9.5	0.75	1	1.207
26	26	0	1	0.009	9.5	0.75	1	1.1845
27	27	0	1	0.009	9.5	0.75	1	1.206
28	28	0	1	0.009	9.5	0.75	1	1.191
29	29	0	1	0.009	9.5	0.75	1	1.209
30	30	0	1	0.009	9.5	0.75	1	1.189
31	31	0	1	0.009	9.5	0.75	1	1.206

cumstance; the CCD results were equipped with a polynomial condition for every reaction. The accompanying quadratic models communicated an experimental relationship in uncoded values among reaction and information factors:

A:1.753-31.6 sorbent amount(g)-0.0679 solution volume (ml) − 0.486n(H2O2)/n(DBT) + 0.1687n(H2O2)/n(DBT)*n(H2O2)/n(DBT) + 35.0 catalyst amount(g)*%amount loading of C-dots − 21.12 catalyst amount(g)*n(H2O2)/n(DBT)-0.03 47 solution volume(ml)*%amount loading of C-dots-0.1275 %amount loading of C-dots*n(H2O2)/n(DBT).

R-sq and R-sq (adj) were obtained 99.31% and 98.71% for modified model, respectively. Table 3 depicts the analysis of variance (ANOVA) calculated for the regression models. The maximum measure of the p-value for lack-of-fit i.e. 0.701 (p-value > 0.05) was estimated for modified parameters. On the basis of the method presented by Derringer and Such

Table3 Electrode preparation factors, obtained by response surface design.

Source	DF[a]	Adj SS[b]	Adj MS[c]	F-Value	p-Value
ANOVA for five experimental					
Linear	4	1.11076	0.277690	547.02	0.000
Square	4	0.04147	0.010367	20.42	0.000
Residual error	21	0.00575	0.00027		
Lack-of-fit	16	0.00812	0.000508	0.71	0.701
Pure error	6	0.00373	0.000621		
Total	30	1.17665			

[a] Degrees of freedom.
[b] Adjusted sum of squares.
[c] Adjusted mean squares.

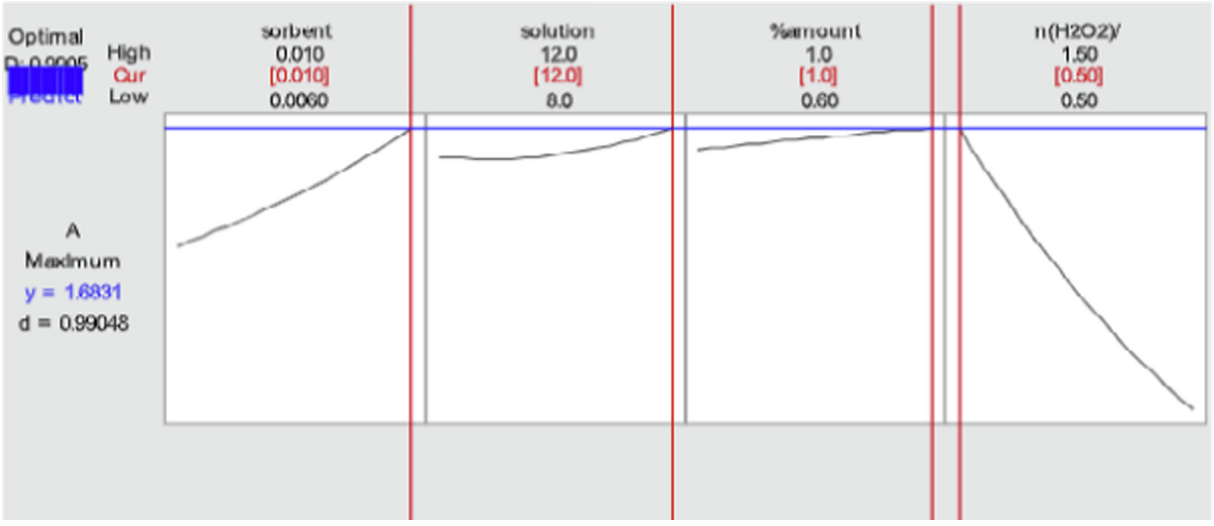

Fig. 8 Interpretation of residual graphs.

(Tarley et al., 2009), the optimum points were obtained at 0.01 g, 12 cm3, 0.5, and 1% for catalyst amount, solution volume, n (H2O2)/n (DBT), and % concentration of C-dots, respectively. Concerning C-dots, when the C-dots loading got optimized to 1%, the ODS system showed the best desulfurization capacity. At the ideal conditions, the anticipated reactions of conditions and reactions to the connected attractive quality, desulfurization technique were performed. In the ideal condition, the expected desulfurization percentage was equivalent to 98.13%, and the concentration of the DBT residues was equal to 1.87 ppm. In the optimal condition, the anticipated content of sulfur reduced with g-BN was equal to 60%, and the DBT was declined to 40 mg/L.

3.5.3. Interpretation of residual graphs

One procedure of testing for an ordinary dispersion is to decide how intently the focus on a typical likelihood plot complies with a direct line. Minitab typically gives the standard probability plot directly as portrayed in Fig. 8. The usual probability plot is a helpful instrument for indicating the normal distribution of residuals. The points pursue a straight line in this plot. From this test, it is clear that the data has normally been distributed. Residual study (the difference between the experimental and the predicted value) is an important component in model interpretation. For an excellent model, the residuals should be distributed randomly and normally. In Fig. 8, the plot of residuals against the fitted qualities is given and the residuals don't clarify a specific example and are roughly normally conveyed. The histogram in Fig. 8 shows a dispersion of estimations around the symmetrical means with the majority of the estimations grouped around the focal point of the diagram proposing a typical circulation without anomaly of the residuals. The final graph of the residual against the order of observation is balanced and centered near-zero without a clear outline of the order of observation.

4. Conclusion

C-dots were wrapped in g-BN which has been made using a primary single-step in situ process, and their execution for OADS of the unmanageable natural sulfur compound DBT in the oil stage with watery H2O2. Sizes of C-dots can be controlled in the scope of about 4–5 nm. High desulfurization effectiveness of 93.5% could be framed with a lower proportion of H2O2/DBT as 0.5 which is not demonstrating the exact stoichiometric measure of H2O2.C-dots demonstrated

phenomenal synergist impact in this H2O2 oxidized response as an advertiser in the impetus H2O2 can be viably deteriorated using the cooperation with C-dots to create. OH claims unprecedented oxidative movement. The extra way provided by C-dots for the use of H2O2 assumed an imperative job to the decrease of the invalid debasement of H2O2. Furthermore, g-BN additionally provides synergic impact bringing about a high reactant action. C-dots could open up potential roads for research as a compelling nano test.

Declaration of Competing Interest

The authors declare that they have no known competing financial interests or personal relationships that could have appeared to influence the work reported in this paper.

Acknowledgement

The authors thank Payame Noor University for providing research facilities.

References

Baker, S.N., Baker, G.A., 2010. Luminescent carbon nanodots: emergent nanolights. Angew. Chem. Int. Ed 49, 6726.

Calvaruso, G., Minore, A., Liveri, V.T., 2001. FT-IR investigation of the urea state in AOT reversed micelles. J. Colloid Interface Sci. 243, 227–232.

Chen, G.X., Hong, M.H., Chong, T.C., Elim, H.I., Ma, G.H., Ji, W., 2004. Controlled fabrication of ultrathin-shell BN hollow spheres with excellent performance in hydrogen storage and wastewater treatment. J. Appl. Phys. 95, 1455.

Chen, X., Jia, Z., Huang, F., Diazo, J., Liu, H., 2021. Atomically dispersed metal catalysts on nanodiamond and its derivatives: synthesis and catalytic application. Chem. Commun. 57, 11591–11603.

Corso, M., Auwarter, W., Muntwiler, M., Tamai, A., Greber, T., Osterwalder, J., 2004. Boron nitride nanomesh. Science 303, 217.

Dean, C.R., Young, A.F., Meric, I., Lee, C., Wang, L., Sorgenfrei, S., et al, 2010. Boron nitride substrates for high-quality graphene electronics. Nat. Nanotech. 5, 722–726.

Gaddam, R.R., Vasudevan, D., Narayan, R., Raju, K.V.S.N., 2014. Controllable synthesis of biosourced blue-green fluorescent carbon dots from camphor for the detection of heavy metal ions in water. RSC Adv. 4, 57137–57143.

Gholinejad, M., Seyedhamzeh, M., Razeghi, M., Najera, C., Kompany-Zareh, M., 2016. Iron oxide nanoparticles modified with carbon quantum nanodots for the stabilization of palladium nanoparticles: an efficient catalyst for the suzuki reaction in aqueous media under mild conditions. Chem. CAT Chem. 8, 441–447.

Hinde, C.S., Ansovini, D., Wells, P.P., Collins, G., Van Aswegen, S., Holmes, J.D., Hor, T.S.A., Raja, R., 2015. Elucidating Structure-Property Relationships in the Design of Metal Nanoparticle Catalysts for the Activation of Molecular Oxygen. ACS Catal. 5, 3807–3816.

Huang, F., Deng, Y., Chen, Y., Cai, X., Peng, M., Jia, Z., Ren, P., Xiao, D., Wen, X., Wang, N., Liu, H., Ma, D., 2018. Atomically Dispersed Pd on Nanodiamond/Graphene Hybrid for Selective Hydrogenation of Acetylene. J. Am. Chem. Soc. 140, 13142–13146.

Huang, X.Q., Li, X.Y., Zou, M.C., Song, S., Tang, C.H., Yuan, Y., Jiao, N., 2014. From ketones to esters by a Cu-catalyzed highly selective C (CO)–C (alkyl) bond cleavage: Aerobic oxidation and oxygenation with air. J. Am. Chem. Soc. 136, 14858–14865.

Huang, L., Qi, J., Wu, X., Wu, W., Jiang, H., 2013. Aerobic Oxidative Coupling between Carbon Nucleophiles and Allylic Alcohols: A Strategy to Construct β-(Hetero) Aryl Ketones and Aldehydes through Hydrogen Migration. Chem. Eur. J 19, 15462–15466.

Jawale, D.V., Gravel, E., Shah, N., Dauvois, V., Li, H., Namboothiri, I.N.N., Doris, E., 2015. ooperative Dehydrogenation of N-Heterocycles Using a Carbon Nanotube-Rhodium Nanohybrid. Chem. Eur. *J* 21, 7039–7042.

Kannan, R., Jang, H.-R., Yoo, E.-S., Lee, H.-K., Yoo, D.J., 2015. Facile green synthesis of palladium quantum dots@ carbon on mixed valence cerium oxide/graphene hybrid nanostructured bifunctional catalyst for electrocatalysis of alcohol and water. RSC Adv. 5, 35993–36000.

Kennedy, M., Krouse, D., 1999. Strategies for improving fermentation medium performance. J. Ind. Microbiol. Biotechnol 23, 456–475.

Lei, W.W., Liu, D., Chen, Y., 2015. Highly Crumpled boron nitride nanosheets as adsorbents:scalable solvent-less production. Adv. Mater. Interf. 2, 1400529.

Lian, G., Zhang, X., Zhang, S., Liu, D., Cui, D., Wang, Q., 2012. Controlled fabrication of ultrathin-shell BN hollow spheres with excellent performance in hydrogen storage and wastewater treatment. Energy Environ. Sci 5, 7072–7080.

Liu, D., He, L., Lei, W., Klika, K.D., Kong, L., Chen, Y., 2015. Multifunctional polymer/porous boron nitride nanosheet membranes for superior trapping emulsified oils and organic molecules. Adv. Mater. Interfaces 2, 1500228.

Liu, J., Liu, Y., Liu, N.Y., Han, Y.Z., Zhang, X., Huang, H., Lifshitz, Y., Lee, S.T., Zhong, J., Kang, Z.H., 2015. Metal-free efficient photocatalyst for stable visible water splitting via a two-electron pathway. Science 347, 970–974.

Liu, X., Xiao, J., Ding, H., Zhong, W., Xu, Q., Su, S., Yin, D., 2016. Catalytic aerobic oxidation of 5-hydroxymethylfurfural over VO2 + and Cu2+ immobilized on amino functionalized SBA-15. Chem. Eng. J. 283, 1315–1321.

Liu, F., Yu, J., Ji, X.X., Qian, M.Q., 2015. Nanosheet-structured boron nitride spheres with aversatile adsorption capacity for water cleaning. ACS Appl. Mater. Inter. 7, 1824–1832.

Meng, F.C., Peng, M., Chen, Y., Cai, X., Huang, F., Yang, L., Liu, X., Li, T., Wen, X., Wang, N., Xiaog, D., Jiang, H., Xia, L., Liu, H., Ma, D., 2022. Defect-rich graphene stabilized atomically dispersed Cu3 clusters with enhanced oxidase-like activity for antibacterial applications. Appl. Catal. B. 301, 120826.

Miyamura, H., Min, H., Soule, J.F., Kobayashi, S., 2015. Size of gold nanoparticles driving selective amide synthesis through aerobic condensation of aldehydes and amines. Angew. Chem. International Edition 54, 7564–7567.

Nag, A. et al, 2010. Graphene Analogues of BN: Novel Synthesis and Properties. ACS Nano 4, 1539–1544.

Nag, A., Raidongia, K., Hembram, K.P.S.S., Datta, R., Waghmare, U.V., Rao, C.N.R., 2010. Graphene analogues of BN: novel synthesis and properties. ACS Nano 4, 1539–1544.

Pakdel, A., Bando, Y., Golberg, D., 2014. Nano boron nitride flatland. Chem. Soc. Rev 43, 934–959.

Pan, D., Zhang, J., Li, Z., Wu, C., Yana, X., Wu, M., 2010. Observation of pH-, solvent-, spin-, and excitation-dependent blue photoluminescence from carbon nanoparticles. Chem. Commun 46, 3681.

Peak III, D., Luther, G.W., Sparks, D.L., 2003. spectroscopic studies of boric acid adsorption on hydrous ferric oxide. Geochim. Cosmochim. Acta 67, 2551–2560.

Plackett, R.L., Burman, J.P., 1946. The design of optimum multifactorial experiments. Biometrika 33, 305–325.

Rappas, A.S., 2002. Unipure Corporation, Process for removing low amounts of organic sulfur from hydrocarbon fuels. U.S. Patent No. 6,402,940. 11 Jun. 2002US Patents US 6,402,940; US 6, 406,616, Wachs WO 03/051798.

Sainsbury, T., Satti, A., May, P., Wang, Z., McGovern, I., Gun'ko, Y. K., Coleman, J., 2012. Oxygen radical functionalization of boron nitride nanosheets. J. Am. Chem. Soc. 134, 18758–18771.

Sampanthar, J.T., Rong, X., Dautzenberg, F.M., 2004. PCT Patent Application PCT/SG2004/000160.

Sharif, K.M., Rahman, M.M., Azmir, J., 2014. Experimental design of supercritical fluid extraction–A review. J. Food Eng. 124, 105–116.

Tarley, C.R.T., Silveira, G., dos Santos, W.N.L., 2009. hemometric tools in electroanalytical chemistry: methods for optimization based on factorial design and response surface methodology. Microchem. J. 92, 58–67.

Tian, L., Ghosh, D., Chen, W., Pradhan, S., Chang, X.J., Chen, S.W., 2009. Nanosized carbon particles from natural gas soot. Chem. Mater 21, 2803–2809.

Tu, W.F., Chin, Y.H., 2015. Catalytic consequences of chemisorbed oxygen during methanol oxidative dehydrogenation on Pd clusters. ACS Catal. 5, 3375–3386.

Wang, X., Zhang, J., Zou, W., Wang, R., 2015. Facile synthesis of polyaniline/carbon dot nanocomposites and their application as a fluorescent probe to detect mercury. RSC Adv. 5, 41914–41919.

Wang, X.B., Zhi, C.Y., Li, L., Zeng, H.B., Li, C., Mitome, M., Golberg, D., Bando, Y., 2011. "Chemical Blowing" of Thin-Walled Bubbles: High-Throughput Fabrication of Large-Area, Few-Layered BN and Cx-BN Nanosheets. Adv. Mater. 23, 4072–4076.

Wen, G., Diao, J., Wu, S., Yang, W., Schoegl, R., Su, D.S., 2015. Acid properties of nanocarbons and their application in oxidative dehydrogenation. ACS Catal 5, 3600–3608.

Weng, Q., Wang, X., Zhi, C., Bando, Y., Golberg, D., 2013. Boron nitride porous microbelts for hydrogen storage. ACS Nano 7, 1558–1565.

Weng, Q.H., Wang, X.B., Bando, Y., Golberg, D., 2014. Controlled fabrication of ultrathin-shell BN hollow spheres with excellent performance in hydrogen storage and wastewater treatment. Adv. Energy Mater. 4, 1301525.

Weng, Q.H., Wang, X.B., Bando, Y., Golberg, D., 2014. One-Step Template-Free Synthesis of Highly Porous Boron Nitride Microsponges for Hydrogen Storage. Energy Mater 4, 1301525.

Wu, P., Zhu, W., Chao, Y., Zhang, J., Zhang, P., Zhu, H., Li, C., Chen, Z., Li, H., Dai, S., 2016. A template-free solvent-mediated synthesis of high surface area boron nitride nanosheets for aerobic oxidative desulfurization. Chem. Commun 52, 144–147.

Xiao, F., Chen, Z., Casillas, G., Richardson, C., Li, H., Huang, Z., 2016. Controllable synthesis of few-layered and hierarchically porous boron nitride nanosheets. Chem. Commun. 52, 3911–3914.

Xiong, J., Zhu, W., Li, H., Ding, W., Chao, Y., Wu, P., Li, H., 2015. Graphene-like boron nitride induced remarkable adsorption capacity for dibenzothiophene in fuels. Green Chem. 17, 1647–1656.

Xiong, J., Zhu, W., Li, H., Ding, W., Chao, Y., Wu, P., Xun, S., Zhang, M., Li, H., 2015. Few-layered graphene-like boron nitride induced a remarkable adsorption capacity for dibenzothiophene in fuels. Green Chem 17, 1647–1656.

Xu, B.R., Lumb, J.P., Arndtsen, B.A., 2015. Angew, A TEMPO-Free Copper-Catalyzed Aerobic Oxidation of Alcohols. Angew. Chem. Int. Ed. 54, 4208–4211.

Xu, X.Y., Ray, R., Gu, Y.L., Ploehn, H.J., Gearheart, L., Raker, K., Scrivens, W.A., 2004. Electrophoretic analysis and purification of fluorescent single-walled carbon nanotube fragments. J. Am. Chem. Soc. 126, 12736–12737.

Yang, X., Huang, C., Fu, Z., Song, H., Liao, S., Su, Y., Du, L., Li, X., 2013. n effective Pd-promoted gold catalyst supported on mesoporous silica particles for the oxidation of benzyl alcohol. Appl. Catal. B: Environ 140, 419–425.

Yu, X., Cohen, S.M., 2015. Photocatalytic metal–organic frameworks for the aerobic oxidation of arylboronic acids. Chem. Commun 51, 9880–9883.

Zhang, J., Qiao, Z.A., Mahurin, S.M., Jiang, X., Chai, S.H., Lu, H., Nelson, K., Dai, S., 2015. Hypercrosslinked Phenolic Polymers with Well-Developed Mesoporous Frameworks. Angew. Chem. Int. Ed 54, 4582–4586.

Zhang, Y., Wang, R., 2018. Synthesis of silica@C-dots/phosphotungstates core-shell microsphere for effective oxidative-adsorptive desulfurization of dibenzothiophene with less oxidant. Appl. Catal. B 234, 247–259.

Zhi, C.Y., Bando, Y., Tang, C.C., Kuwahara, H., Golberg, D., 2009. Large-scale fabrication of boron nitride nanosheets and their utilization in polymeric composites with improved thermal and mechanical properties. Adv. Mater. 21, 2889–2893.

Zhi, C., Bando, Y., Tang, C., Kuwahara, H., Golberg, D., 2013. Large-scale fabrication of boron nitride nanosheets and their utilization in polymeric composites with improved thermal and mechanical properties. Adv. Mater 21, 2889–2893.

Zhong, W., Kirk, S.R., Yin, D., Li, Y., Zou, R., Mao, L., Zou, G., 2015. Solvent-free selective oxidation of toluene by oxygen over MnOx/SBA-15 catalysts: Relationship between catalytic behavior and surface structure. Chem. Eng. J. 280, 737–747.

Zhu, J., Wang, T., Xu, X., Xiao, P., Li, J., 2013. Pt nanoparticles supported on SBA-15: Synthesis, characterization and applications in heterogeneous catalysis. Appl. Catal. B 130, 197–217.

Zolgharnein, J., Shahmoradi, A., Ghasemi, J.B., 2013. Doehlert matrix for multivariate optimization of Pb (II) adsorption onto Robinia tree leaves. Chemometr. J. 27, 12–20.